scientific reports

OPEN

The effect of laser pulse evolution on down-ramp injection in laser wakefield accelerators

Arohi Jain[1,3], Samuel R. Yoffe[2,3], Bernhard Ersfeld[2], George K. Holt[2], Devki Nandan Gupta[1]✉ & Dino A. Jaroszynski[2]✉

Electron self-injection in laser wakefield accelerators (LWFAs) is an important determinator of electron beam parameters. Controllable and adjustable LWFA beams are essential for applications. Controlled injection by capturing sheath electrons can be achieved using plasma density down-ramps or bumps, which perturb the LWFA bubble phase velocity by varying the plasma frequency and by affecting relativistic self-focussing of the laser. We report on a comprehensive study, using particle-in-cell simulations, of the effect of laser pulse evolution on injection on density perturbations. We show how the LWFA can be optimised to make it suitable for use in a wide range of applications, in particular those requiring short duration, low slice-emittance and low energy spread, and high-charge electron bunches.

The rapid development of laser wakefield accelerators (LWFAs)[1] is attracting the interest of research communities because of their potential as compact tools for scientific discovery and applications in energy, healthcare, manufacturing etc. High charge, high-energy electron bunches[2] are used in radiobiology, radiotherapy, pharmaceutics, chemistry, and industrial radiography[3–6]. High-quality, high-energy electron beams from LWFAs[2,7–12] are potential next-generation compact light sources[13], such as ultra-compact X-ray free-electron lasers (FELs) and brilliant betatron sources[14–18], which have many applications including X-ray imaging[4,19], material structure analysis, diagnostics in high energy density physics[20,21], photolithography and tumour treatment[22]. Electron beams can also be used to produce high photon energy bremsstrahlung radiation for high contrast industrial and medical imaging applications[23]. Most of these applications require stable, reproducible, high-quality, and energy tunable electron beams with a range of different characteristics.

The accelerating fields of a LWFA are produced by the ponderomotive force of an ultrashort intense laser pulse, which displaces plasma electrons and excites a near-luminal plasma wave with an associated wakefield that has a characteristic length equal to the plasma wavelength $\lambda_p = 2\pi c/\omega_p$, where $\omega_p = \sqrt{n_e e^2/(m_e \varepsilon_0)}$ is the plasma frequency and e, m_e, and n_e the electron charge, mass, and density, respectively. Particles are accelerated to high energies in millimetres to centimetres[1,24]. In the nonlinear LWFA "bubble" regime, the intense driver laser causes near-total cavitation of plasma electrons in the trailing wake, which results in fields exceed several hundreds of GV/m[25]. Self-injection of plasma electrons into this field can occur when the laser pulse power exceeds the critical power for relativistic self-focusing[26], $P > 17.4(\lambda_p/\lambda)^2$ GW[27], where λ is the laser wavelength. Self-phase modulation leads to self-steepening[28], self-compression, which results in variations of the group velocity of the laser pulse[29], and deformation and elongation of the bubble. This directly affects electron self-injection and beam quality; mismatch of the laser pulse in its self-guiding structure can cause oscillations of its spot size, resulting in modifications to both the bubble size and its phase velocity.

Numerous methods for self-injection of electrons into the laser wakefield have been investigated for producing low-emittance, high-brightness electron beams, mainly based on analysis of particle-in-cell (PIC) simulations[30–32]. A promising technique is ionization induced injection, where inner-shell electrons are ionized near the peak of the laser pulse at a potential that results in injection and trapping inside the wakefield[33–39]. Another interesting injection method is colliding pulse injection, where the ponderomotive force of colliding pulses boosts the electron velocity to the bubble velocity[40], which results in energy tuneable electron beams, but this is experimentally challenging as it requires alignment and synchronization of laser pulses. However, a very simple injection method, proposed by Bulanov et al.[41], takes advantage of a brief reduction of the bubble velocity while the laser propagates through a downward density ramp[30]. For longer density transitions (length

[1]Department of Physics and Astrophysics, University of Delhi, Delhi 110 007, India. [2]Department of Physics, SUPA and University of Strathclyde, Glasgow G4 0NG, UK. [3]These authors contributed equally: Arohi Jain and Samuel R. Yoffe. ✉email: dngupta@physics.du.ac.in; d.a.jaroszynski@strath.ac.uk

of the down-ramp), $L_{tr} > \lambda_p$, the local phase velocity v_p of the plasma wave in a one-dimensional model can be expressed as[42–44]

$$v_p = v_g \left(1 + \frac{\zeta}{2n_e}\frac{dn_e}{dz}\right)^{-1}, \tag{1}$$

where v_g is the laser group velocity, $\zeta = z - v_g t$ is the spatial coordinate in the frame co-moving with the laser pulse and $n_e(z)$ is the plasma density. The phase velocity of the plasma wave behind the laser pulse is reduced briefly in a downward density gradient ($dn_e/dz < 0$ and $\zeta < 0$ behind the laser pulse), which enables efficient and controllable trapping of electrons. Electrons displaced at an earlier time oscillate at a higher plasma frequency (because of the higher density) and cross the back of the bubble at a time when the plasma frequency has decreased, thus appearing in the accelerating structure. As a result, a significant fraction of electrons can be trapped in the wakefield by the end of the density transition. For sharp density transitions, where $L_{tr} < \lambda_p$ and the plasma density reduces from n_1 to n_2, the change in the plasma wavelength by the end of a density transition is given by $\Delta\lambda_p = \lambda_p[1 - (n_1/n_2)^{1/2}]$[45]. Injected electrons are located at a similar phase of the wake, have similar initial energy, and are exposed to the same accelerating field, which results in a quasi mono-energetic beam. The required density profile can be created by a razor blade that partially intercepts a supersonic gas jet to create a narrow shock front with a sharp drop in density ($< \lambda_p$)[46–48] or multiple intercepting gas jets[49]. The down-ramp injection technique for beam-driven wakefield accelerators[50–54] and the LWFA[55,56] has been extensively studied for generating high-quality electron beams with attosecond duration electron bunches[57].

The properties of injected electron bunches depend on the evolution of the laser pulse in the plasma[48,57,58]. Recent experiments and PIC simulations suggest that this is due to non-linear lengthening of the plasma wave[59], which depends on both the peak laser intensity and its waist, and to variations of the wake phase velocity, which are a function of the laser vector potential $a_0 = eE_L/(m_e\omega c)$[57,60], where E_L is the electric field amplitude and ω the laser angular frequency. In addition, the front part of the laser pulse loses energy to the wakefield as it propagates due to photon deceleration[61] and diffraction, which results in laser etching and reduction of its group velocity[62]. It is therefore expected that changes in the wake phase velocity at the density down-ramp will be influenced by the laser amplitude. As a_0 evolves the increased ponderomotive force will result in displacement of more charge, when forming the wake, and more momentum will be transferred to electrons that form the sheath. Both the wakefield bubble size[57,63] and the sheath electron trajectories[64] strongly depend on the laser pulse intensity. Thus, a larger number of electrons will be injected for higher a_0. We will show that variations in the laser pulse over the down-ramp strongly affect the injected charge and its phase-space distribution. The precise position of the down-ramp region becomes an important and readily adjustable parameter that can be used to optimise the electron bunch properties because of the spatio-temporal evolution of the laser pulse.

Here we use PIC numerical simulations to investigate the role of laser pulse evolution and plasma density profile on injection, for both density bumps and single down-ramps, as shown in Fig. 1. The properties of accelerated electron bunches are analysed as a function of the position, length and peak density of the down-ramp region, to establish the optimal conditions for producing high-quality beams, and more generally for controlling electron bunch properties, such as energy, charge, and total and slice emittance and energy spread. Both average (integrated) and slice values of parameters are calculated because they give a more comprehensive insight into the intrinsic quality of the self-injected electron bunches. This provides a reliable and simple method of optimising electron beam parameters for applications. We show that the minimum slice energy spread of 0.5% can be achieved for peak current of 5–6 kA and normalised slice emittance as small as 0.05 π mm mrad.

Results

Particle-in-cell (PIC) simulations have been performed (see "Methods") to evaluate the influence of selected plasma density profiles on injection. We first consider a density bump with a relative peak height, α, above the background density, and bump length L, as illustrated in Fig. 1a. The profile is chosen to have sinusoidal up- and down-ramps of length $0 \le R \le L$, where $R = 0$ defines a top-hat, flat-top, bump (dashed) and $R = L$ defines a fully-smoothed bump with no plateau (solid). The injected bunch characteristics are explored by varying the bump position, height, length and ramp length. To ensures the same initial laser evolution for all relative density

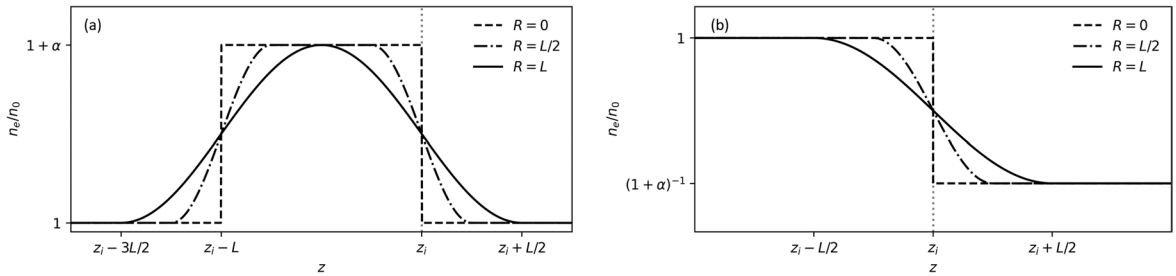

Figure 1. Density shapes. (**a**) Schematic showing a density bump of relative height α and length L, with the down-ramp region aligned at z_i (indicated by the vertical dotted line). As the ramp length, $0 \le R \le L$, is increased and the bump profile is smoothed, while maintaining a constant full width at half height, which is aligned with position z_i. (**b**) A single down-ramp positioned at z_i, and density n_0 drops to $n_0/(1+\alpha)$, with the density midpoint aligned with z_i.

drops, α, we also investigate a single density down-ramp, as illustrated in Fig. 1b, where the density drops from a plateau at n_0 to a plateau at $n_0/(1+\alpha)$. However, the lower density plateau after the transition has an impact on subsequent acceleration due to lower accelerating fields and higher bubble phase velocities for the three different values of ramp lengths, L.

Figure 2a,b shows the evolution of a_0 and the laser waist size for bump positions $z_i = 300\,\mu$m and $z_i = 800\,\mu$m, respectively. The evolution of the laser pulse is identical up to the position where it encounters the bump. It continues to be self-focussed as it propagates through the higher density plasma bump resulting in a slight increase in the laser amplitude causing more charge to be displaced, which leads to an increase in the injected charge. Electrons also gain additional momentum from the increased ponderomotive force due to the higher intensity laser pulse, which contributes to an increase in injected charge[60].

The evolution of the laser pulse results in a dependence of the electron bunch properties on the injection position, which is illustrated in Fig. 2c for single down-ramps (with $R = 0$ and $\alpha = 0.3$) positioned at different z_i. The evolution of laser pulses is identical until the point of injection, after which the drop in plasma density alters the subsequent evolution of the laser pulse because of relativistic self-focusing. Without a down-ramp, the laser pulse self-focusses to $a_0 \simeq 4$ at around $z = 0.8$ mm. Self focussing is reduced for an earlier density drop position, z_i, as the laser pulse propagates mainly in the lower density plasma and therefore reaches a lower maximum intensity at a slightly earlier time. In contrast, injection for later z_i increases the injected charge because of the increase in a_0 at the time of injection (indicated by the vertical lines). Electron bunches injected near to or beyond the laser focal position experience a contraction of the bubble due to the decreasing laser intensity, and therefore the back of the bubble can catch up with and partially overtake the electron bunch[62]. When a_0 is large the plasma bubble size increase[65] results in deceleration of the rear of the bunch and acceleration of its front, increasing the overall energy spread and emittance. Figure 2d shows the energy spectra 1 mm after injection, for four different injection positions, where we only record energies above $E_{\text{thresh}} = 20$ MeV (vertical dashed line). The properties of injected electrons depend indirectly on a_0 through positioning of the down-ramp. In the following sections, we discuss the electron bunch properties for both density bump and single down-ramp cases.

Bump injection

A density modulation or bump can be used to precipitate injection by changing the phase velocity of the back of the bubble[57]. An up-ramp causes the plasma wavelength to decrease and the bubble to contract, which increases the velocity of its back thus suppressing injection. In contrast, on a down-ramp the bubble expands, which decreases its velocity. The density gradient (height and ramp length) determines the bubble velocity, see Eq. (1), which is confirmed by simulation data.

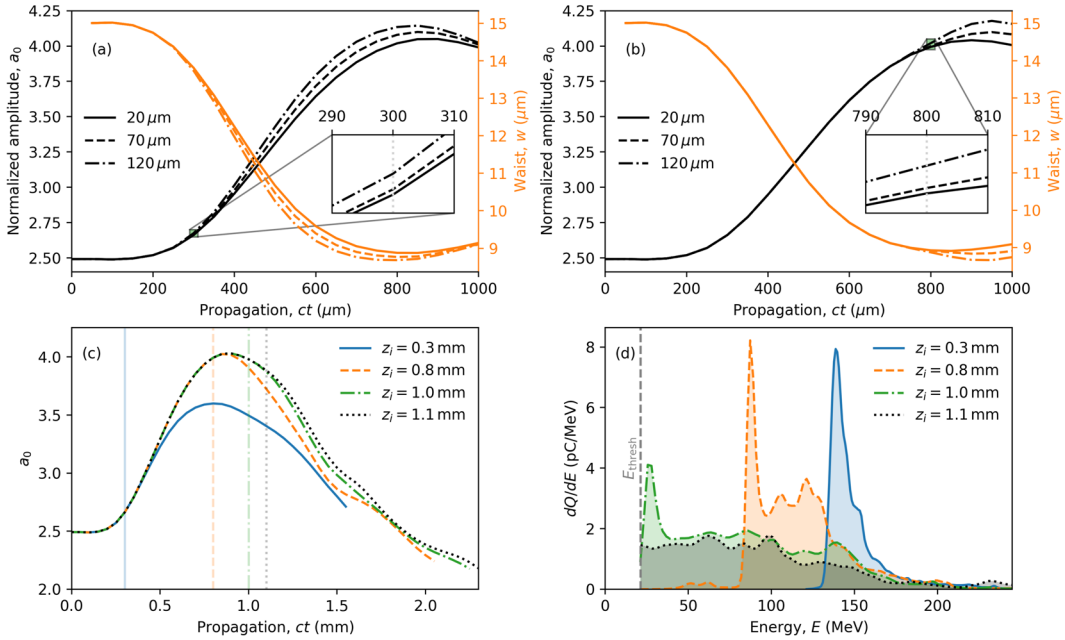

Figure 2. Laser pulse evolution dependence on bump length and ramp position. (**a**) and (**b**) illustrate the evolution of the laser pulse for bumps with $L = 20, 70, 120\,\mu$m (solid, dashed, dot-dashed, respectively). Self-focussing of the laser pulse is enhanced with increase in bump length. The inset shows the down-ramp region magnified for (**a**) $z_i = 300\,\mu$m and (**b**) $z_i = 800\,\mu$m. (**c**) illustrates the evolution of the laser pulse amplitude, a_0, for a single ($\alpha = 0.3$) down-ramp with $R = 0$ located at position z_i (vertical lines). The laser pulse self-focuses in the initial higher-density region, resulting in a larger a_0 for later injection positions. (**d**) Electron energy spectra 1 mm after injection for various ramp positions, z_i.

To investigate how the bunch characteristics depend on the density bump parameters, we have varied the ramp length (R), bump length, height and position of the density bump. We begin by varying R, in Fig. 3, which presents (a) the injected charge, (b) the maximum energy (E_{max}) and average energy ($\langle E \rangle$), and (c) the r.m.s. energy spread (ΔE) and relative energy spread ($\Delta E/\langle E \rangle$). These data are calculated 700 μm after injection for a density bump of relative height $\alpha = 0.3$ at position $z_i = 300\,\mu$m. The results show that all three quantities (charge, energy, and energy spread) can be tuned almost linearly with ramp length, R. Within the ramp length range explored, the injected charge reduces significantly from $R = 0$ to $R = 50\,\mu$m, as the change in the plasma wavelength does not cause the velocity of the back of the bubble (v_p) to reduce significantly (refer to Eq. (1)) so that fewer electrons meet the requirements for injection. As a result, injected bunches have a lower current for $R = 25$ and $50\,\mu$m, as shown in Fig. 3e.

The bunch lengths for different ramp lengths R in Fig. 3e are: $\sigma_{FWHM} = 0.9\,\mu$m, $\sigma_{rms} = 2.3\,\mu$m ($R = 0\,\mu$m); $\sigma_{FWHM} = 1.2\,\mu$m, $\sigma_{rms} = 2.2\,\mu$m ($R = 25\,\mu$m); $\sigma_{FWHM} = 0.9\,\mu$m, $\sigma_{rms} = 1.5\,\mu$m ($R = 50\,\mu$m). Here, σ_{FWHM} and σ_{rms} represent full-width half maximum and root mean square width, respectively. High charge bunches strongly deform the accelerating field through beam loading[66,67] and their average energy decreases as the charge increases. This is clearly observed when comparing the cases $R = 0, 25, 50\,\mu$m in Fig. 3d. Other important properties calculated for electrons located within thin transverse slices, such as the slice longitudinal emittance ($\varepsilon_/^{\parallel}$), slice average energy ($\langle E_/ \rangle$), relative slice energy spread ($\Delta E_/ / \langle E_/ \rangle$), and slice transverse emittance ($\varepsilon_/^{\perp}$), are shown in Fig. 3f–i and their values for the lowest slice energy spread are shown in Table 1.

The energy spread is higher around the high current region of the electron bunch, and the average slice energy spread for $R = 0,\ 25$, and $50\,\mu$m is $\Delta E_/ / \langle E_/ \rangle = 3.09\%$, 1.42%, and 0.81%, where $\langle E_/ \rangle = 128.7$, 154.5, and 193.5 MeV, respectively. The reduced density gradient due to increasing R suppresses injection of electrons with lower longitudinal velocities caused by large transverse momenta. Therefore, the transverse slice emittance is lower for longer ramp lengths. In contrast, to maximize the charge in the electron bunch, a square bump with sharp density transition ($R = 0$) should be chosen, at the expense of emittance. From Table 1 it can be seen that segments of the electron bunch have excellent slice parameters, e.g. slice energy spread of $\Delta E_/ / \langle E_/ \rangle \approx 0.5\%$, peak current of ≈ 4 kA and transverse slice emittance of $\varepsilon_/^{\perp} \approx 0.05\,\pi$ mm mrad.

Figures 4 and 5 show the electron bunch properties calculated 700 μm after injection at $z_i = 300\,\mu$m and $z_i = 800\,\mu$m, respectively. The latter corresponds to injection near the peak laser amplitude, after which the laser intensity drops. We see that the position z_i has a clear impact on the injected charge – the increased laser amplitude at the point of injection leads to more charge. For $z_i = 300\,\mu$m (Fig. 4) increasing the bump length

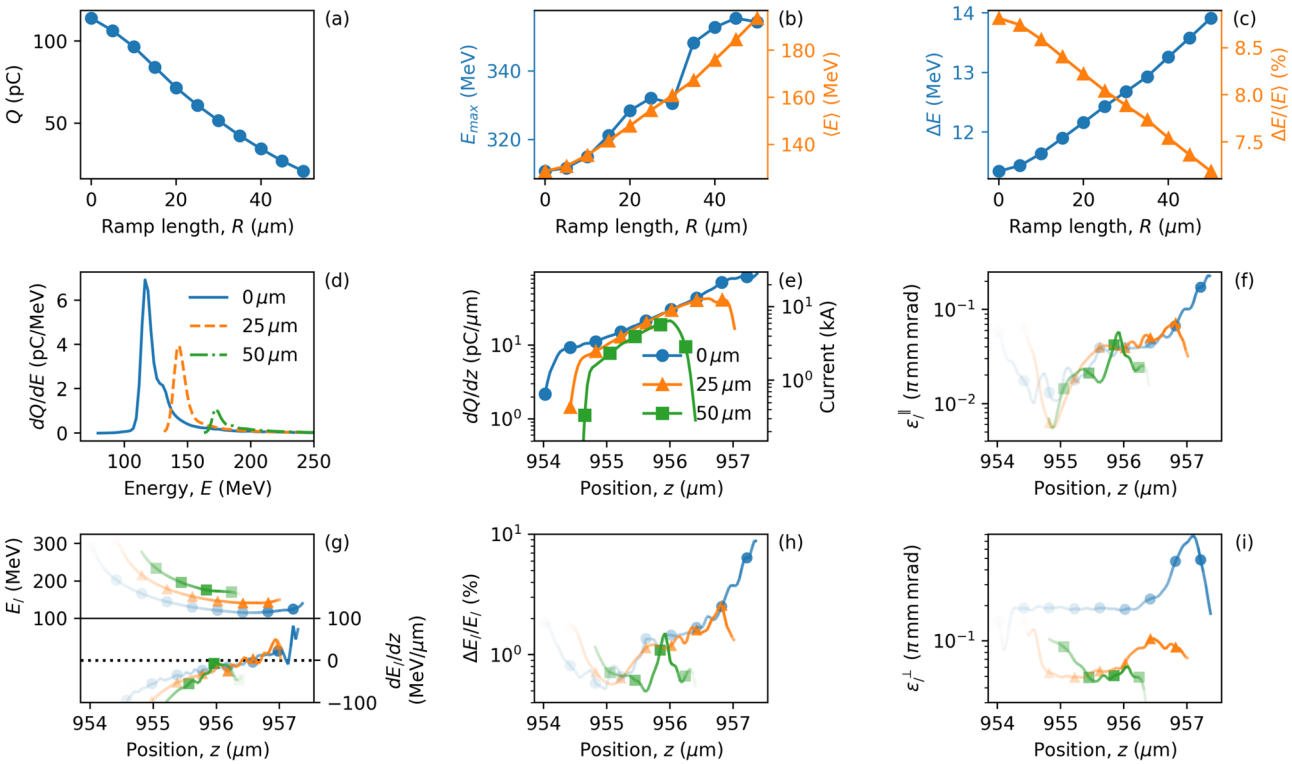

Figure 3. Effect of ramp length on bunch properties. Electron bunch properties for injection at $z_i = 300\,\mu$m, while varying the ramp length, R. (**a**–**c**) show the variation of the injected charge, energy, and energy spread, respectively. Data points indicated by circles correspond to the left axis, and triangles to the right axis. Panels (**d**,**e**) show the energy spectra and charge distribution, respectively, for three ramp lengths, $R = 0, 25, 50\,\mu$m. Properties in narrow transverse slices of electrons are presented in panels (**f**–**i**), where opacity indicates charge and the same legend as in panel (**e**) is used to identify lines. Properties are calculated at $ct = 1$ mm (700 μm after injection).

Ramp length, R [μm]	Figure 3h pos. of min. $\Delta E_f/\langle E_f\rangle$ [μm]	Figure 3h $\Delta E_f/\langle E_f\rangle$ [%]	Figure 3g E [MeV]	Figure 3g dE/dz [MeV/μm]	Figure 3e dQ/dz [pC/μm]	Figure 3e Current [kA]	Figure 3f $\varepsilon_f^{\parallel}$ [π mm mrad]	Figure 3i $\varepsilon_f^{\perp}$ [π mm mrad]
0	955.0	0.52	156	− 50.7	12.68	3.8	0.011	0.19
25	955.1	0.57	188	− 80.4	11.32	3.4	0.012	0.05
50	955.6	0.49	187	− 45.3	15.58	4.7	0.017	0.05

Table 1. Bunch parameters for different ramp lengths from Fig. 3. Slice values, $\Delta E_f/\langle E_f\rangle$, $\varepsilon_f^{\parallel}$ and $\varepsilon_f^{\perp}$, correspond to position where $\Delta E_f/\langle E_f\rangle$ is smallest.

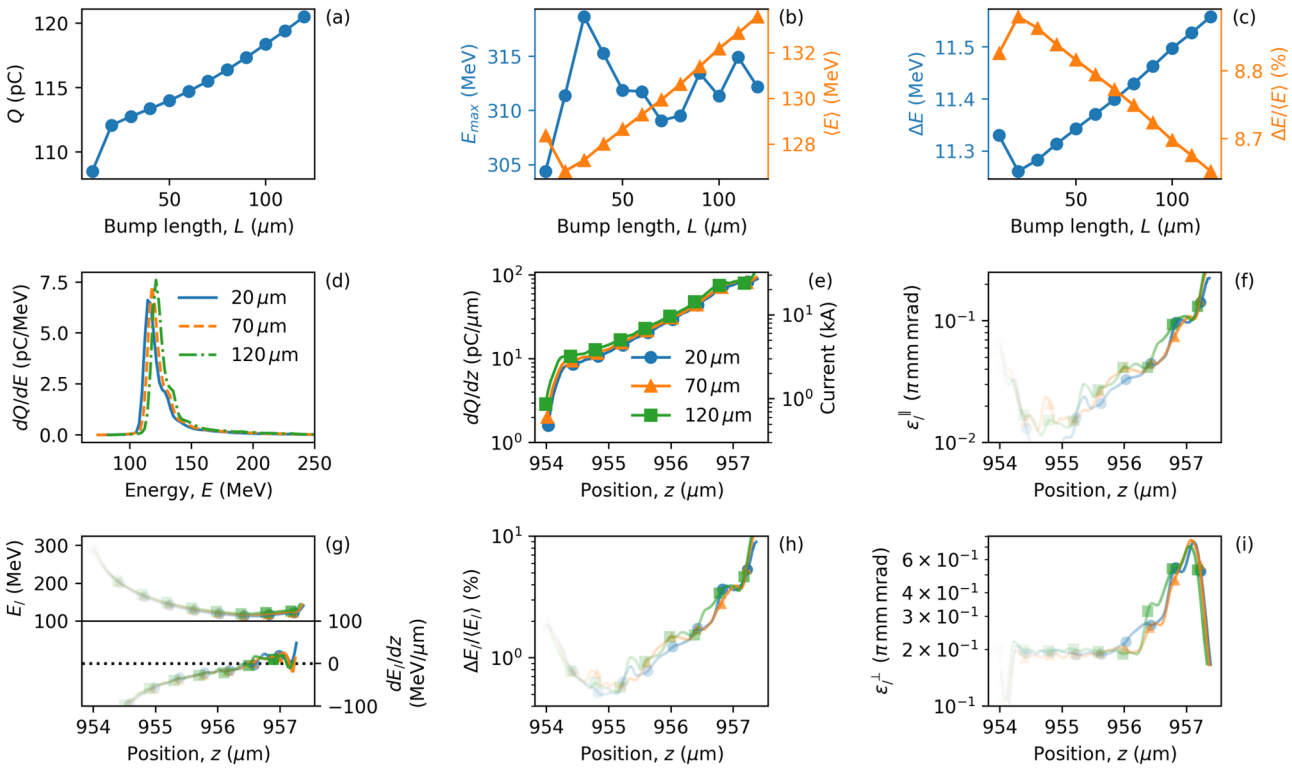

Figure 4. Effect of bump length on bunch properties. Electron bunch properties for injection at $z_i = 300\,\mu$m with varying bump length and fixed bump height, $\alpha = 0.3$. Panels (**a**–**c**) show the variation of the injected charge, energy, and energy spread, respectively. Data points indicated by circles correspond to the left axis, and triangles to the right axis. Panels (**d**) and (**e**) show the energy spectra and charge distribution, respectively, for three example bump lengths, $L = 20, 70, 120\,\mu$m. Properties of electrons contained in narrow transverse slices are presented in panels (**f**–**i**), where opacity is used to indicate charge and the same legend as panel (**e**) is used to identify lines. Properties are calculated at $ct = 1$ mm (700 μm after injection).

corresponds to an increase in a_0 and an increase in injected charge. In contrast, for $z_i = 800\,\mu$m (Fig. 5) increasing the bump length ($L > 20\,\mu$m) causes a decrease in injected charge. In comparison, Figs. 4b and 5b also show how injection further along the laser evolution produces lower average electron energy and larger emittance, shown in Figs. 4f–i and 5f–i. Note that higher average energies are usually obtained for lower charge where beam loading is smaller. Depending on the electron bunch shape, beam loading can increase or decrease the energy spread, as different parts of the bunch experience different accelerating fields. In Fig. 4e, bunch lengths hardly change for different bump lengths of $L = 20, 70, 120\,\mu$m, with $\sigma_{FWHM} = 0.8\,\mu$m and $\sigma_{rms} = 2.2\,\mu$m. Similarly, in Fig. 5e, the bunch length is constant for varying bump lengths, with $\sigma_{FWHM} = 0.5\,\mu$m and $\sigma_{rms} = 2.6\,\mu$m. Additionally, the properties of electron bunch slices for different bump lengths are similar in both Figs. 4 and 5. This implies that the bunch properties depend more on the down-ramp gradient of the bump than the length of the bump, as expected. The large difference in the bunch properties observed in Figs. 4 and 5 indicates that the injection point itself can be used as a parameter to modify the electron bunch properties. Tables 2 and 3 show electron bunch parameters corresponding to Figs. 4 and 5, respectively, where the slice values correspond to the position where the slice energy spread is smallest, $\Delta E_f/\langle E_f\rangle \approx 0.5\%$, in Table 2 corresponding to a peak current of 3–5 kA and normalised transverse slice emittance, $\varepsilon_f^{\perp} \approx 0.2\pi$ mm mrad. Table 3 shows similar values but with higher current. To explore this further, a parameter scan is performed by varying the two bump parameters most easily manipulated in an experiment—the height and position of the bump (refer to Supplementary Fig. S1). The

Bump length, L [μm]	Figure 4h pos. of $\Delta E_/ / \langle E_/ \rangle$ [μm]	Figure 4h $\Delta E_/ / \langle E_/ \rangle$ [%]	Figure 4g E [MeV]	Figure 4g dE/dz [MeV/μm]	Figure 4e dQ/dz [pC/μm]	Figure 4e Current [kA]	Figure 4f $\varepsilon_/^{\parallel}$ [π mm mrad]	Figure 4i $\varepsilon_/^{\perp}$ [π mm mrad]
20	954.9	0.49	161	− 61.4	10.99	3.3	0.007	0.20
70	955.2	0.56	148	− 45.9	14.92	4.5	0.014	0.19
120	955.1	0.52	151	− 37.5	16.29	4.9	0.013	0.20

Table 2. Bunch parameters for different bump lengths from Fig. 4. Slice values, $\Delta E_/ / \langle E_/ \rangle$, $\varepsilon_/^{\parallel}$ and $\varepsilon_/^{\perp}$, correspond to position where $\Delta E_/ / \langle E_/ \rangle$ is smallest.

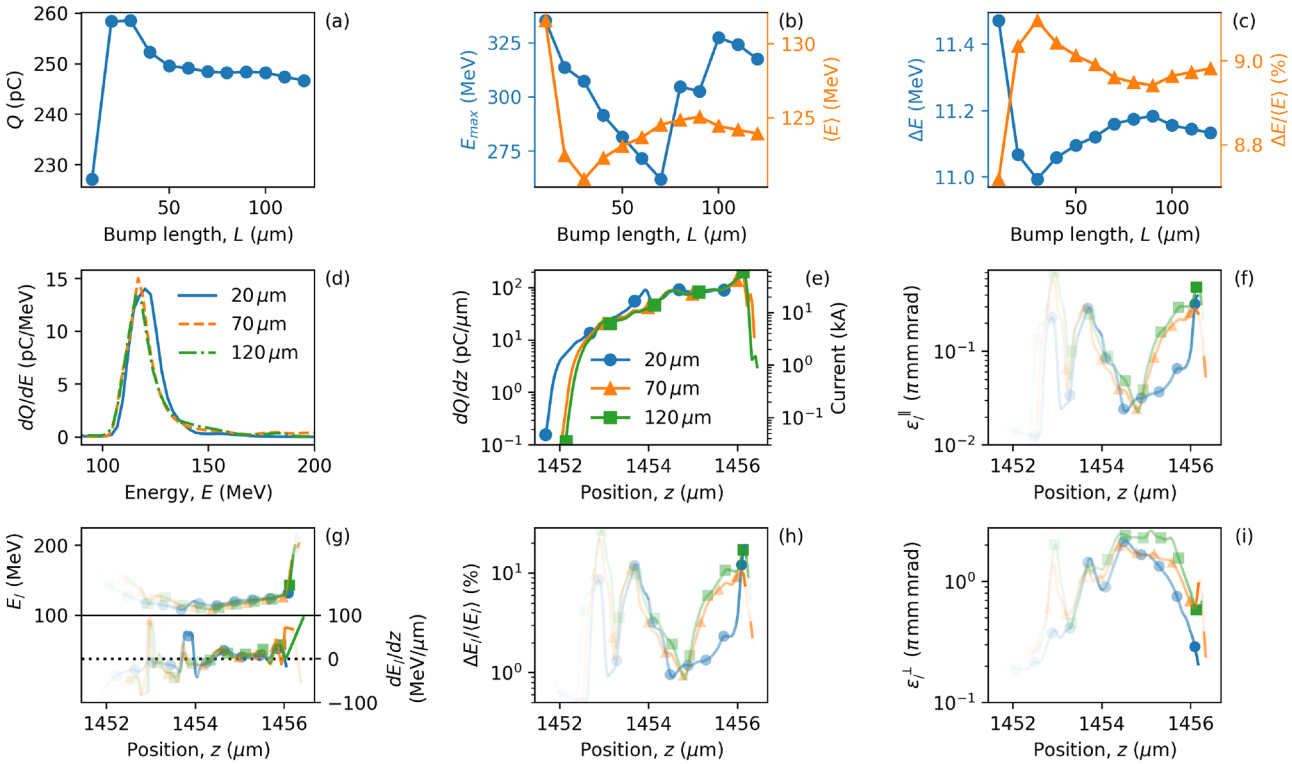

Figure 5. Effect of injection point on bunch properties. As Fig. 4 but for electrons injected at $z_i = 800\,\mu$m and properties calculated at $ct = 1.5$ mm (700 μm after injection).

Bump length [μm]	Figure 5h pos. of $\Delta E_/ / \langle E_/ \rangle$ [μm]	Figure 5h $\Delta E_/ / \langle E_/ \rangle$ [%]	Figure 5g E [MeV]	Figure 5g dE/dz [MeV/μm]	Figure 5e dQ/dz [pC/μm]	Figure 5e Current [kA]	Figure 5f $\varepsilon_/^{\parallel}$ [π mm mrad]	Figure 5i $\varepsilon_/^{\perp}$ [π mm mrad]
20	1453.1	0.91	117	− 12.4	23.42	7.0	0.024	0.34
	1454.5	0.89	114	8.4	86.66	26.0	0.023	2.15
70	1453.2	1.33	127	− 19.2	24.69	7.4	0.038	0.52
	1454.8	0.94	116	3.5	75.85	22.7	0.024	1.70
120	1453.3	1.75	128	− 30.4	22.77	6.8	0.049	0.43
	1454.8	0.85	116	6.2	74.91	22.5	0.022	2.30

Table 3. Bunch parameters for different bump lengths from Fig. 5. Slice values, $\Delta E_/ / \langle E_/ \rangle$, $\varepsilon_/^{\parallel}$ and $\varepsilon_/^{\perp}$, correspond to position where $\Delta E_/ / \langle E_/ \rangle$ is smallest.

importance of laser evolution has been discussed in the context of electron self-injection in the LWFA[45,47,57,68], but here we demonstrate that the laser evolution can be used as an extra control parameter for tuning the parameters of plasma-based electron accelerators.

Single down-ramp injection

Supplementary Fig. S1 shows analogous behaviour to that shown in Fig. 3. The highest charge is injected for the shortest ramp length, and as the gradient is reduced by increasing R the injected charge also reduces (c). The response of the bubble to the slower change in density causes a smaller change in the velocity of its back, which results in capture of less charge. The reduction in charge for longer ramps, in turn, leads to higher electron energy (d), in addition to lower slice spread (h) and slice emittance (f),(i). The decrease of electron energy with increasing charge for shorter ramps, as observed in Supplementary Fig. S1b,d, is explained by beam-loading reducing the accelerating field. The bunch lengths for different ramp lengths R in Supplementary Fig. S1e are: $\sigma_{FWHM} = 1.4\,\mu\text{m}$, $\sigma_{rms} = 3.2\,\mu\text{m}$ ($R = 0\,\mu\text{m}$); $\sigma_{FWHM} = 0.8\,\mu\text{m}$, $\sigma_{rms} = 2.6\,\mu\text{m}$ ($R = 25\,\mu\text{m}$); $\sigma_{FWHM} = 1.4\,\mu\text{m}$, $\sigma_{rms} = 2.0\,\mu\text{m}$ ($R = 50\,\mu\text{m}$). This shows an increase in the electron bunch duration for shorter ramp lengths. Shorter ramps also tend to have higher slice energy spread (Supplementary Fig. S1h) because of increased beam loading. For ramp length $R > 25\,\mu\text{m}$, the transverse emittance $\varepsilon_{/}^{\perp}$ remains less than $\sim 1\,\pi$ mm mrad, shown in Supplementary Fig. S1f. For $R = 0$, slice emittance is larger than the other two cases as electrons with larger transverse momentum are trapped due to the rapid change in bubble length similar to that in Fig. 3. Supplementary Table S1 shows the electron bunch parameters corresponding to Supplementary Fig. S1. the slice energy spread is $\Delta E_{/}/\langle E_{/}\rangle \approx 0.5\%$ and corresponding peak current ≈ 5 kA and slice emittance $\varepsilon_{/}^{\perp} \approx 0.1$–$0.4\,\pi$ mm mrad.

The evolution of the laser pulse in the plasma introduces a strong dependence of the accelerated electron bunch properties on the injection position. This is shown in the bump injection case by comparing Figs. 4 and 5, as well as explicitly in Supplementary Fig. S3. The impact of the down-ramp position on the evolution of the laser pulse is noteworthy. In the down-ramp case, the evolution is identical until the point of injection. However, at the injection point, the reduction in plasma density changes relativistic self-focusing and therefore the evolution of the laser pulse (as shown in Supplementary Fig. S4).

Figure 6a shows that the electron bunch injected at $z_i = 1$ mm undergoes a dephasing-like process, which leads to a reduction in energy and an increase in energy spread. An initially accelerated electron bunch is clearly identified (see Fig. 6b) before most of the charge begins to decelerate. Panel (c) shows that the bunch has not reached dephasing at the centre of the bubble, but rather the back of the bubble overtakes most of the bunch. This contraction is caused by the reduction in a_0 after the laser passes its focus, and in Fig. 6c we observe a smaller bubble with a weaker laser wakefield (compared to b). The wake also exhibits features of beam loading, as the high-charge bunch previously contained within the stronger laser wakefield now drives a comparable (if not stronger) wakefield that appears as a cone-like structure extending beyond the rear of the laser wake. The larger part of the bunch is now located in the decelerating field behind the bubble, while the front continues to be accelerated. This introduces a large energy spread as observed at later times in (a) and Fig. 2d.

In Supplementary Fig. S2, we show the evolution of electron bunch properties with respect to the injection position. The values in the shaded region ($z_i > 1$ mm) can not be determined precisely as most of the charge is decelerated below the energy selection threshold 20 MeV (as in Fig. 2d). Supplementary Figure S2a shows the total injected charge. For a given single down-ramp, the change of a_0 with the injection position z_i plays a key role in the injection: higher values of a_0 yield a higher injected charge. The increase in injected charge can be explained by several effects arising from the change in the laser amplitude: The ponderomotive force of the laser on the electrons increases with a_0, which enlarges the bubble[69] and displaced electron volume, as well as imparting larger momentum to electrons. The larger bubble leads to higher field strengths and maximum energy of injected electrons. However, beam loading due to the increase in charge typically lowers the mean energy, as shown in Supplementary Fig. S2b,e, and, by deforming the electric field distribution, increases the energy spread, as shown in Supplementary Fig. S2c. Supplementary Table S2 shows the minimum slice parameters for Supplementary Fig. S2, where the slice energy spread of $\Delta E_{/}/\langle E_{/}\rangle \approx 0.5\%$ at 165 MeV bunch can be achieved with a peak current of ≈ 6 kA and a slice transverse emittance, $\varepsilon_{/}^{\perp} \approx 0.5\,\pi$ mm mrad. It is worth noting that the bunch duration ($\sigma_{rms} = 3.0\,\mu\text{m}$) remains almost constant with increasing injected charge, thus we are able to tune the bunch charge by varying the injection position z_i, while maintaining its duration. As expected, the slice energy spread in Supplementary Fig. S2h and the slice emittance in (f) and (i) are both reduced for lower injected charge. To extend the investigation on bunch properties, a parameter scan is performed by varying the down-ramp parameters (Supplementary Fig. S4)

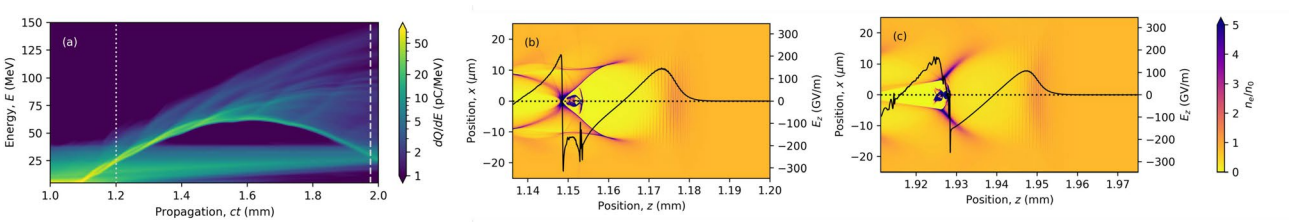

Figure 6. Energy spectrum evolution. (**a**) presents the time evolution of the electron energy spectrum, clearly showing an accelerated bunch that then undergoes a dephasing-like transition. (**b**) The density and on-axis accelerating field shortly after injection (indicated by the dotted line in (**a**)), while (**c**) shows that this bunch is then overtaken by the back of the bubble, with the majority of the bunch located in the decelerating phase ($E_z > 0$) of the wakefield (at the time indicated by the dashed line in (**a**)). The very front of the bunch continues to be accelerated, introducing the large energy spread at later times, observed in (**a**).

The above discussion indicates that the injected charge can be indirectly controlled by tuning the laser a_0 through choice of the position of the down-ramp. However, if a density down-ramp is used to trigger injection after the laser focus, where the amplitude is dropping, then the bubble size reduces and the electron bunch can experience a dephasing-like process at the back of the bubble. The advantage is that this places the front of the bunch in a very high field to attain a much higher maximum energy, but with the consequence that the average energy and energy spread of the whole bunch are much worse. In this regard, a more stable or guided laser evolution might be beneficial for acceleration to high energy over long lengths[70]. When choosing the laser parameters, it is important to ensure that the laser does not cause self-injection before the stimulated injection (beam loading can then help suppress further dark current), which places restrictions on the choice of laser and plasma parameters.

Overall, we show the possibility of tailoring the parameters of the electron bunches produced in LWFAs by tuning the down-ramp height as well as the injection point. We demonstrate that the amount of charge, the bunch length, and the emittance can be controlled by changing the height and position of the down-ramp, which is experimentally easier than changing its shape. From this parameter scan, we can determine optimum parameters for various applications of the LWFA.

Conclusion

We have presented a study of a method of producing high-quality electron bunches using self-injection at a density bump and a single down-ramp. We show that the electron bunch properties can be tuned by varying the plasma density bump/ramp-length, position, and height. For square bump ($R = 0$), we observe increased electron injection and better quality bunches can be obtained by tuning the bump height and position. We have shown how the injection position determines the electron bunch charge and depends on the evolution of the laser pulse a_0. To ensure identical laser evolution up to the point of injection, we have performed simulations for single down-ramp injection. Simulations for different density bump lengths suggest that the electron bunch properties are predominantly influenced by the position of the down-ramp gradient rather than by the bump length. Parameter scans are plotted for large data sets and thus precise parameters can be obtained according to the requirements. In the parameter scan for height α and injection position z_i, regions of lower average slice emittance and slice energy spread give preferred parameters for applications. With this analysis we show that an efficient strategy can be found for controlling the electron bunch parameters—charge, energy, emittance and energy spread. We show that the slice energy spread can be $\Delta E_{/}/\langle E_{/}\rangle < 0.5\%$ at 165 MeV, and with a peak current of ≈ 6 kA and slice emittance as small as $\varepsilon_{/}^{\perp} \approx 0.05\,\pi$ mm mrad. If the emittance can be preserved during subsequent acceleration a much smaller energy spread can be achieved. This could make LWFAs suitable for driving XUV and X-ray FELs using a simple and controllable self-injection scheme.

We anticipate that taking into account laser pulse evolution in optimization and control of self-injection to produce high-quality electron bunches may be crucial for developing compact coherent light sources. Bump and down-ramp parameters enable good control over electron bunch properties. The determination of precise parameter values will require further studies to address the varying requirements of different applications and accommodate available experimental conditions.

Methods

We have performed a series of simulations using the quasi-3D PIC code FBPIC[71], which uses cylindrical geometry and azimuthal modal decomposition to represent the 3D domain. In larger simulation domains and for longer propagation, PIC algorithms can be very computationally demanding and are subject to substantial numerical artifacts. Spectral field solvers, as used by FBPIC, exhibit no spurious numerical dispersion or numerical Cherenkov radiation, and can significantly reduce other forms of numerical noise that arise using finite difference schemes. The simulations included three modes ($m = 0, 1, 2$), and a $z \times r = 63.76\,\mu\text{m} \times 80\,\mu\text{m}$ moving window travelling at the speed of light (in vacuum, c), with grid cell size $\Delta z = \Delta r = 40$ nm and (3,2,12) macro-particles per cell in (z,r,θ). The plasma target has a plateau electron density $n_0 = 3 \times 10^{18}$ cm^{-3} and 100 µm sinusoidal entrance and exit ramps. A linearly-polarized Gaussian laser pulse with wavelength $\lambda = 800$ nm, normalized amplitude $a_0 = 2.5$, waist $w_0 = 15\,\mu$m, and full-width at half-maximum pulse duration 33 fs, propagates along the z-axis and is focussed at the bottom of the up-ramp to the plasma plateau. The laser parameters are chosen to minimize self-injection (total charge $Q < 0.1$ pC) during the interaction with the flat-top plasma (low dark current) despite the laser self-focusing to around $a_0 \sim 4$.

Data availibility

Data associated with research published in this paper is available at: https://doi.org/10.15129/7b3da154-f717-4b15-8118-abe3828c7c56.

Received: 11 December 2023; Accepted: 31 July 2024
Published online: 19 August 2024

References

1. Tajima, T. & Dawson, J. M. Laser electron accelerator. *Phys. Rev. Lett.* **43**, 267–270. https://doi.org/10.1103/PhysRevLett.43.267 (1979).
2. Brunetti, E. *et al.* Low emittance, high brilliance relativistic electron beams from a laser-plasma accelerator. *Phys. Rev. Lett.* **105**, 215007. https://doi.org/10.1103/PhysRevLett.105.215007 (2010).
3. Kneip, S. *et al.* X-ray phase contrast imaging of biological specimens with femtosecond pulses of betatron radiation from a compact laser plasma wakefield accelerator. *Appl. Phys. Lett.* **99**, 093701. https://doi.org/10.1063/1.3627216 (2011).

4. Wenz, J. *et al.* Quantitative x-ray phase-contrast microtomography from a compact laser-driven betatron source. *Nat. Commun.* **6**, 7568. https://doi.org/10.1038/ncomms8568 (2015).
5. Subiel, A. *et al.* Challenges of dosimetry of ultra-short pulsed very high energy electron beams. *Phys. Med.* **42**, 327–331. https://doi.org/10.1016/j.ejmp.2017.04.029 (2017).
6. Kokurewicz, K. *et al.* Focused very high-energy electron beams as a novel radiotherapy modality for producing high-dose volumetric elements. *Sci. Rep.* **9**, 10837. https://doi.org/10.1038/s41598-019-46630-w (2019).
7. Mangles, S. P. D. *et al.* Monoenergetic beams of relativistic electrons from intense laser-plasma interactions. *Nature* **431**, 535–538. https://doi.org/10.1038/nature02939 (2004).
8. Geddes, C. G. R. *et al.* High-quality electron beams from a laser wakefield accelerator using plasma-channel guiding. *Nature* **431**, 538–541. https://doi.org/10.1038/nature02900 (2004).
9. Faure, J. *et al.* A laser-plasma accelerator producing monoenergetic electron beams. *Nature* **431**, 541–544. https://doi.org/10.1038/nature02963 (2004).
10. Wiggins, S. *et al.* High quality electron beams from a laser wakefield accelerator. *Plasma Phys. Controlled Fusion* **52**, 124032. https://doi.org/10.1088/0741-3335/52/12/124032 (2010).
11. Gonsalves, A. J. *et al.* Petawatt laser guiding and electron beam acceleration to 8 gev in a laser-heated capillary discharge waveguide. *Phys. Rev. Lett.* **122**, 084801. https://doi.org/10.1103/PhysRevLett.122.084801 (2019).
12. Aniculaesei, C. *et al.* The acceleration of a high-charge electron bunch to 10 GeV in a 10-cm nanoparticle-assisted wakefield accelerator. *Matter Radiat. Extremes* **9**, 014001. https://doi.org/10.1063/5.0161687 (2023). https://pubs.aip.org/aip/mre/article-pdf/doi/10.1063/5.0161687/18286148/014001_1_5.0161687.pdf.
13. Yang, X., Brunetti, E. & Jaroszynski, D. A. High-energy coherent terahertz radiation emitted by wide-angle electron beams from a laser-wakefield accelerator. *New J. Phys.* **20**, 043046. https://doi.org/10.1088/1367-2630/aab74d (2018).
14. Jaroszynski, D. A. & Vieux, G. Coherent Radiation Sources Based on Laser Plasma Accelerators. *AIP Conf. Proc.* **647**, 902–914. https://doi.org/10.1063/1.1524946 (2002).
15. Huang, Z., Ding, Y. & Schroeder, C. B. Compact x-ray free-electron laser from a laser-plasma accelerator using a transverse-gradient undulator. *Phys. Rev. Lett.* **109**, 204801. https://doi.org/10.1103/PhysRevLett.109.204801 (2012).
16. Schlenvoigt, H.-P. *et al.* A compact synchrotron radiation source driven by a laser-plasma wakefield accelerator. *Nat. Phys.* **4**, 130–133. https://doi.org/10.1038/nphys811 (2008).
17. Cipiccia, S. *et al.* Gamma-rays from harmonically resonant betatron oscillations in a plasma wake. *Nat. Phys.* **7**, 867–871. https://doi.org/10.1038/nphys2090 (2011).
18. Feng, K. *et al.* Free-electron lasing at 27 nanometres based on a laser wakefield accelerator. *Nature* **595**, 516–520. https://doi.org/10.1038/s41586-021-03678-x (2021).
19. Döpp, A. *et al.* Quick x-ray microtomography using a laser-driven betatron source. *Optica* **5**, 199–203. https://doi.org/10.1364/OPTICA.5.000199 (2018).
20. Mahieu, B. *et al.* Probing warm dense matter using femtosecond X-ray absorption spectroscopy with a laser-produced betatron source. *Nat. Commun.* **9**, 3276. https://doi.org/10.1038/s41467-018-05791-4 (2018).
21. Wood, J. *et al.* Ultrafast imaging of laser driven shock waves using betatron x-rays from a laser wakefield accelerator. *Sci. Rep.* **8**, 11010. https://doi.org/10.1038/s41598-018-29347-0 (2018).
22. Oppelt, M. *et al.* Comparison study of in vivo dose response to laser-driven versus conventional electron beam. *Radiat. Environ. Biophys.* **54**, 155–166. https://doi.org/10.1007/s00411-014-0582-1 (2015).
23. Cole, J. M. *et al.* High-resolution μct of a mouse embryo using a compact laser-driven x-ray betatron source. *Proc. Natl. Acad. Sci.* **115**, 6335–6340. https://doi.org/10.1073/pnas.1802314115 (2018).
24. Malka, V. Laser plasma accelerators. *Phys. Plasmas* **19**, 055501. https://doi.org/10.1063/1.3695389 (2012).
25. Pukhov, A. & Meyer-Ter-Vehn, J. Laser wake field acceleration: the highly non-linear broken-wave regime. *Appl. Phys. B: Lasers Opt.* **74**, 355–361. https://doi.org/10.1007/s003400200795 (2002).
26. Gupta, D. N., Hur, M. S., Hwang, I., Suk, H. & Sharma, A. K. Plasma density ramp for relativistic self-focusing of an intense laser. *J. Opt. Soc. Am. B* **24**, 1155–1159. https://doi.org/10.1364/JOSAB.24.001155 (2007).
27. Esarey, E., Schroeder, C. B. & Leemans, W. P. Physics of laser-driven plasma-based electron accelerators. *Rev. Mod. Phys.* **81**, 1229–1285. https://doi.org/10.1103/RevModPhys.81.1229 (2009).
28. Vieira, J., Fiúza, F., Silva, L. O., Tzoufras, M. & Mori, W. B. Onset of self-steepening of intense laser pulses in plasmas. *New J. Phys.* **12**, 045025. https://doi.org/10.1088/1367-2630/12/4/045025 (2010).
29. Ren, C. *et al.* Compressing and focusing a short laser pulse by a thin plasma lens. *Phys. Rev. E* **63**, 026411. https://doi.org/10.1103/PhysRevE.63.026411 (2001).
30. Ke, L. T. *et al.* Near-gev electron beams at a few per-mille level from a laser wakefield accelerator via density-tailored plasma. *Phys. Rev. Lett.* **126**, 214801. https://doi.org/10.1103/PhysRevLett.126.214801 (2021).
31. Islam, M. R. *et al.* Near-threshold electron injection in the laser-plasma wakefield accelerator leading to femtosecond bunches. *New J. Phys.* **17**, 093033. https://doi.org/10.1088/1367-2630/17/9/093033 (2015).
32. Götzfried, J. *et al.* Physics of high-charge electron beams in laser-plasma wakefields. *Phys. Rev. X* **10**, 041015. https://doi.org/10.1103/PhysRevX.10.041015 (2020).
33. Chen, M., Sheng, Z.-M., Ma, Y.-Y. & Zhang, J. Electron injection and trapping in a laser wakefield by field ionization to high-charge states of gases. *J. Appl. Phys.* **99**. https://doi.org/10.1063/1.2179194 (2006).
34. Pak, A. *et al.* Injection and trapping of tunnel-ionized electrons into laser-produced wakes. *Phys. Rev. Lett.* **104**, 025003. https://doi.org/10.1103/PhysRevLett.104.025003 (2010).
35. McGuffey, C. *et al.* Ionization induced trapping in a laser wakefield accelerator. *Phys. Rev. Lett.* **104**, 025004. https://doi.org/10.1103/PhysRevLett.104.025004 (2010).
36. Zeng, M., Chen, M., Sheng, Z.-M., Mori, W. B. & Zhang, J. Self-truncated ionization injection and consequent monoenergetic electron bunches in laser wakefield acceleration. *Phys. Plasmas* **21**, 030701. https://doi.org/10.1063/1.4868404 (2014).
37. Zeng, M. *et al.* Multichromatic narrow-energy-spread electron bunches from laser-wakefield acceleration with dual-color lasers. *Phys. Rev. Lett.* **114**, 084801. https://doi.org/10.1103/PhysRevLett.114.084801 (2015).
38. Mirzaie, M. *et al.* Demonstration of self-truncated ionization injection for gev electron beams. *Sci. Rep.* **5**, 14659. https://doi.org/10.1038/srep14659 (2015).
39. Wang, J., Zeng, M., Wang, X., Li, D. & Gao, J. Scissor-cross ionization injection in laser wakefield accelerators. *Plasma Phys. Controlled Fusion* **64**, 045012. https://doi.org/10.1088/1361-6587/ac4853 (2022).
40. Faure, J. *et al.* Controlled injection and acceleration of electrons in plasma wakefields by colliding laser pulses. *Nature* **444**, 737–739. https://doi.org/10.1038/nature05393 (2006).
41. Bulanov, S., Naumova, N., Pegoraro, F. & Sakai, J. Particle injection into the wave acceleration phase due to nonlinear wake wave breaking. *Phys. Rev. E* **58**, R5257–R5260. https://doi.org/10.1103/PhysRevE.58.R5257 (1998).
42. Faure, J., Rechatin, C., Lundh, O., Ammoura, L. & Malka, V. Injection and acceleration of quasimonoenergetic relativistic electron beams using density gradients at the edges of a plasma channel. *Phys. Plasmas* **17**, 083107. https://doi.org/10.1063/1.3469581 (2010).
43. Zhang, C. J. *et al.* Evolution of plasma wakes in density up- and down-ramps. *Plasma Phys. Controlled Fusion* **60**, 024003. https://doi.org/10.1088/1361-6587/aa9d27 (2018).

44. Lee, P. *et al.* Dynamics of electron injection and acceleration driven by laser wakefield in tailored density profiles. *Phys. Rev. Accel. Beams* **19**, 112802. https://doi.org/10.1103/PhysRevAccelBeams.19.112802 (2016).
45. Buck, A. *et al.* Shock-front injector for high-quality laser-plasma acceleration. *Phys. Rev. Lett.* **110**, 185006. https://doi.org/10.1103/PhysRevLett.110.185006 (2013).
46. Swanson, K. K. *et al.* Control of tunable, monoenergetic laser-plasma-accelerated electron beams using a shock-induced density downramp injector. *Phys. Rev. Accel. Beams* **20**, 051301. https://doi.org/10.1103/PhysRevAccelBeams.20.051301 (2017).
47. Tsai, H. E. *et al.* Control of quasi-monoenergetic electron beams from laser-plasma accelerators with adjustable shock density profile. *Phys. Plasmas* **25**. https://doi.org/10.1063/1.5023694 (2018).
48. Zhang, C. *et al.* Effect of fluctuations in the down ramp plasma source profile on the emittance and current profile of the self-injected beam in a plasma wakefield accelerator. *Phys. Rev. Accel. Beams* **22**, 111301. https://doi.org/10.1103/PhysRevAccelBeams.22.111301 (2019).
49. Kornaszewski, A. *et al.* Plasma density shaping for attosecond electron bunch generation. In Jaroszynski, D. A. & Hur, M. (eds.) *Relativistic Plasma Waves and Particle Beams as Coherent and Incoherent Radiation Sources III*, vol. 11036, 110360R, https://doi.org/10.1117/12.2522780. International Society for Optics and Photonics (SPIE, 2019).
50. Martinez de la Ossa, A. *et al.* Optimizing density down-ramp injection for beam-driven plasma Wakefield accelerators. *Phys. Rev. Accel. Beams* **20**, 091301. https://doi.org/10.1103/PhysRevAccelBeams.20.091301 (2017).
51. Xu, X. L. *et al.* High quality electron bunch generation using a longitudinal density-tailored plasma-based accelerator in the three-dimensional blowout regime. *Phys. Rev. Accel. Beams* **20**, 111303. https://doi.org/10.1103/PhysRevAccelBeams.20.111303 (2017).
52. Kurz, T. *et al.* Demonstration of a compact plasma accelerator powered by laser-accelerated electron beams. *Nat. Commun.* **12**, 2895. https://doi.org/10.1038/s41467-021-23000-7 (2021).
53. Cabadağ, J. C. *et al.* Gas-dynamic density downramp injection in a beam-driven plasma wakefield accelerator. *Phys. Rev. Res.* **3**, L042005. https://doi.org/10.1103/PhysRevResearch.3.L042005 (2021).
54. Ullmann, D. *et al.* All-optical density downramp injection in electron-driven plasma wakefield accelerators. *Phys. Rev. Res.* **3**, 043163. https://doi.org/10.1103/PhysRevResearch.3.043163 (2021).
55. Ekerfelt, H., Hansson, M., Gallardo González, I., Davoine, X. & Lundh, O. A tunable electron beam source using trapping of electrons in a density down-ramp in laser wakefield acceleration. *Sci. Rep.* **7**, 12229. https://doi.org/10.1038/s41598-017-12560-8 (2017).
56. Silva, T., Helm, A., Vieira, J., Fonseca, R. & Silva, L. On the use of the envelope model for down-ramp injection in laser-plasma accelerators. *Plasma Phys. Controll. Fusion* **62**, 024001. https://doi.org/10.1088/1361-6587/ab5298 (2019).
57. Tooley, M. P. *et al.* Towards attosecond high-energy electron bunches: Controlling self-injection in laser-wakefield accelerators through plasma-density modulation. *Phys. Rev. Lett.* **119**, 044801. https://doi.org/10.1103/PhysRevLett.119.044801 (2017).
58. Massimo, F., Lifschitz, A. F., Thaury, C. & Malka, V. Numerical studies of density transition injection in laser wakefield acceleration. *Plasma Phys. Controlled Fusion* **59**, 085004. https://doi.org/10.1088/1361-6587/aa717d (2017).
59. Ding, H. *et al.* Nonlinear plasma wavelength scalings in a laser wakefield accelerator. *Phys. Rev. E* **101**, 023209. https://doi.org/10.1103/PhysRevE.101.023209 (2020).
60. Jain, A. & Gupta, D. N. Optimization of electron bunch quality using a chirped laser pulse in laser wakefield acceleration. *Phys. Rev. Accel. Beams* **24**, 111302. https://doi.org/10.1103/PhysRevAccelBeams.24.111302 (2021).
61. Murphy, C. D. *et al.* Evidence of photon acceleration by laser wake fields (vol 13, pg 033108, 2006). *Phys. Plasmas* **13**. https://doi.org/10.1063/1.2218327 (2006).
62. Yoffe, S. R. *et al.* Controlling the group velocity of an intense laser pulse using a pre-pulse. In Jaroszynski, D. A. & Hur, M. (eds.) *Relativistic Plasma Waves and Particle Beams as Coherent and Incoherent Radiation Sources IV*, vol. 11778, 8 – 17, https://doi.org/10.1117/12.2595294. International Society for Optics and Photonics (SPIE, 2021).
63. Benedetti, C., Schroeder, C. B., Esarey, E., Rossi, F. & Leemans, W. P. Numerical investigation of electron self-injection in the nonlinear bubble regime. *Phys. Plasmas* **20**, 103108. https://doi.org/10.1063/1.4824811 (2013).
64. Barber, S. K. *et al.* Measured emittance dependence on the injection method in laser plasma accelerators. *Phys. Rev. Lett.* **119**, 104801. https://doi.org/10.1103/PhysRevLett.119.104801 (2017).
65. Wang, J., Zeng, M., Li, D., Wang, X. & Gao, J. High quality beam produced by tightly focused laser driven wakefield accelerators. *Phys. Rev. Accel. Beams* **26**, 091303. https://doi.org/10.1103/PhysRevAccelBeams.26.091303 (2023).
66. Tzoufras, M. *et al.* Beam loading in the nonlinear regime of plasma-based acceleration. *Phys. Rev. Lett.* **101**, 145002. https://doi.org/10.1103/PhysRevLett.101.145002 (2008).
67. Tzoufras, M. *et al.* Beam loading by electrons in nonlinear plasma wakes. *Phys. Plasmas* **16**, 056705. https://doi.org/10.1063/1.3118628 (2009).
68. Gonsalves, A. J. *et al.* Tunable laser plasma accelerator based on longitudinal density tailoring. *Nat. Phys.* **7**, 862–866. https://doi.org/10.1038/nphys2071 (2011).
69. Lu, W. *et al.* Generating multi-gev electron bunches using single stage laser wakefield acceleration in a 3d nonlinear regime. *Phys. Rev. ST Accel. Beams* **10**, 061301. https://doi.org/10.1103/PhysRevSTAB.10.061301 (2007).
70. Gupta, D. N., Yoffe, S. R., Jain, A., Ersfeld, B. & Jaroszynski, D. A. Propagation of intense laser pulses in plasma with a prepared phase-space distribution. *Sci. Rep.* **12**, 20368. https://doi.org/10.1038/s41598-022-24664-x (2022).
71. Lehe, R., Kirchen, M., Andriyash, I. A., Godfrey, B. B. & Vay, J.-L. A spectral, quasi-cylindrical and dispersion-free particle-in-cell algorithm. *Comput. Phys. Commun.* **203**, 66–82. https://doi.org/10.1016/j.cpc.2016.02.007 (2016).

Acknowledgements

This work is financially supported by the Science and Engineering Research Board, Department of Science & Technology, Government of India (Grant No. CRG/2022/001989). We also acknowledge support from the U.K. EPSRC (grant number EP/N028694/1) and received funding from the European Union's Horizon 2020 research and innovation programme under grant agreement no. 871124 Laserlab-Europe. SRY and BE acknowledge support from the STFC (grant number ST/G008248/1). Results were obtained using the ARCHIE-WeSt High Performance Computer (https://www.archie-west.ac.uk) based at the University of Strathclyde, and the facilities of the N8 Centre of Excellence in Computationally Intensive Research (N8 CIR) provided and funded by the N8 research partnership and EPSRC (grant number EP/T022167/1), coordinated by the Universities of Durham, Manchester and York.

Author contributions

DNG and AJ came up with the idea for the project. SRY carried out the simulations. Discussion, analysis, interpretation, writing and validation was undertaken by AJ, SRY, BE, GKH, DNG and DAJ. SRY and AJ contributed equally.

Competing interests

The authors declare no competing interests.

Additional information

Supplementary Information The online version contains supplementary material available at https://doi.org/10.1038/s41598-024-69049-4.

Correspondence and requests for materials should be addressed to D.N.G. or D.A.J.

Reprints and permissions information is available at www.nature.com/reprints.

Publisher's note Springer Nature remains neutral with regard to jurisdictional claims in published maps and institutional affiliations.

Open Access This article is licensed under a Creative Commons Attribution 4.0 International License, which permits use, sharing, adaptation, distribution and reproduction in any medium or format, as long as you give appropriate credit to the original author(s) and the source, provide a link to the Creative Commons licence, and indicate if changes were made. The images or other third party material in this article are included in the article's Creative Commons licence, unless indicated otherwise in a credit line to the material. If material is not included in the article's Creative Commons licence and your intended use is not permitted by statutory regulation or exceeds the permitted use, you will need to obtain permission directly from the copyright holder. To view a copy of this licence, visit http://creativecommons.org/licenses/by/4.0/.

© The Author(s) 2024